Supporting Information

Colorimetric detection of iron and fluorescent detection of zinc and cadmium by a chemosensor having a bio-friendly octopamine

Ji Hye Kang and Cheal Kim

Department of Fine Chemistry and Department of Interdisciplinary Bio IT Materials, Seoul National University of Science and Technology, Seoul 139-743, Korea. Fax: +82-2-973-9149; Tel: +82-2-970-6693; E-mail: chealkim@seoultech.ac.kr (C. Kim).

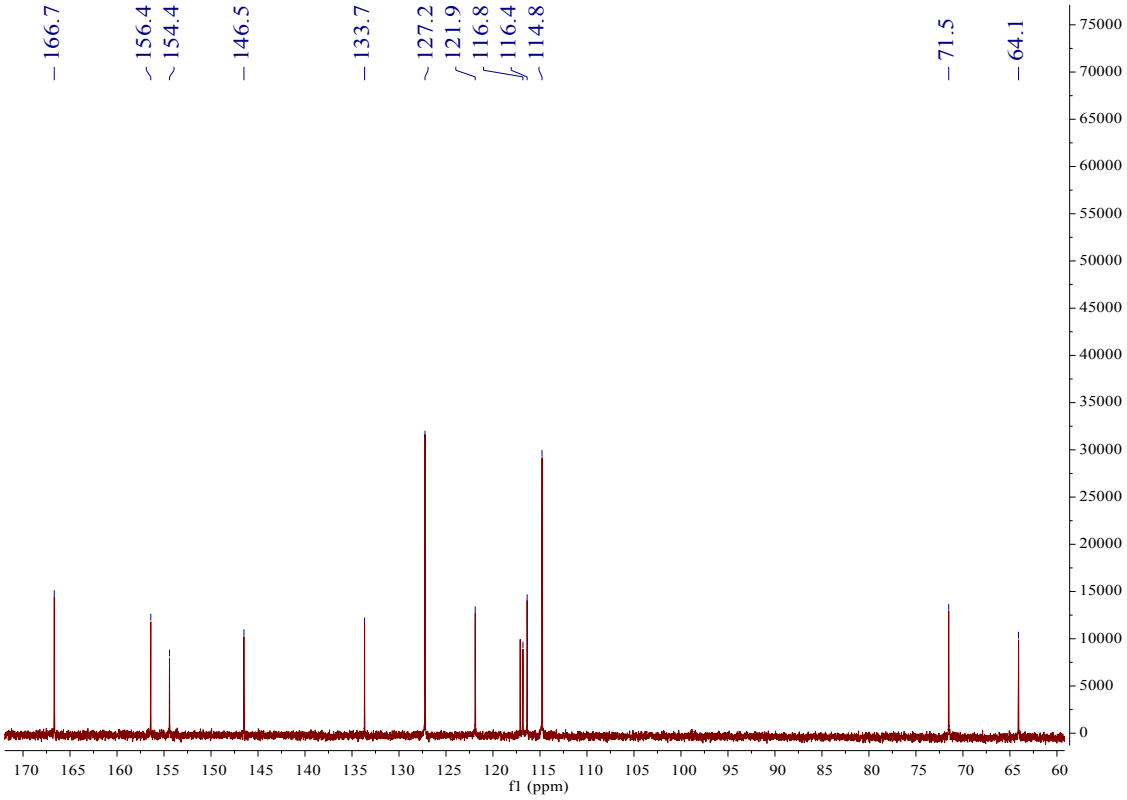

Fig. S1. ^{13}C NMR spectrum of **1**.

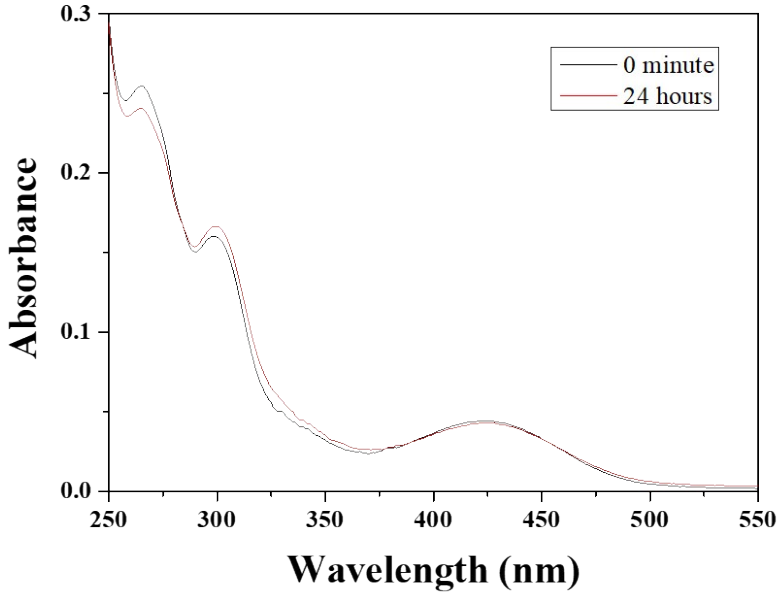

Fig. S2. UV-vis absorption spectra of **1** (20 μM) in MeOH.

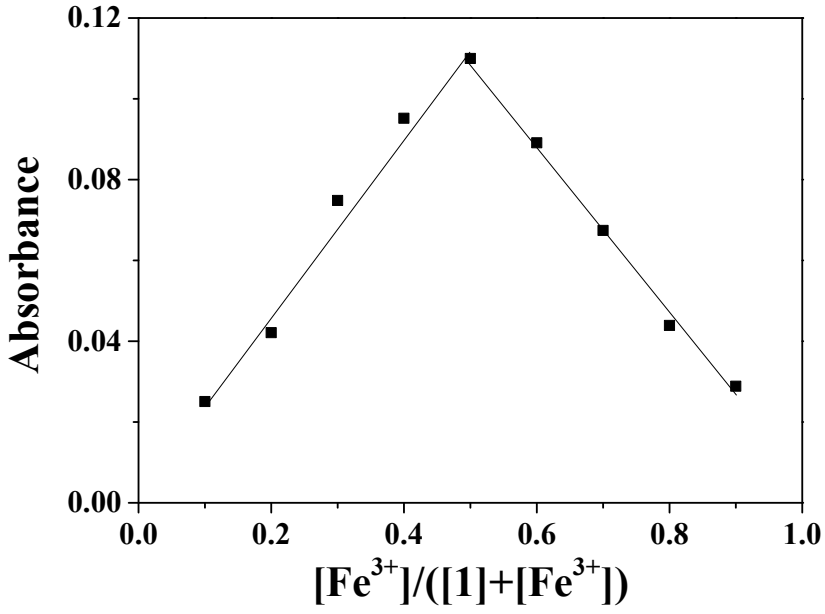

Fig. S3. Job plot for the binding ratio of **1** (80 μM) toward Fe^{3+} (80 μM).

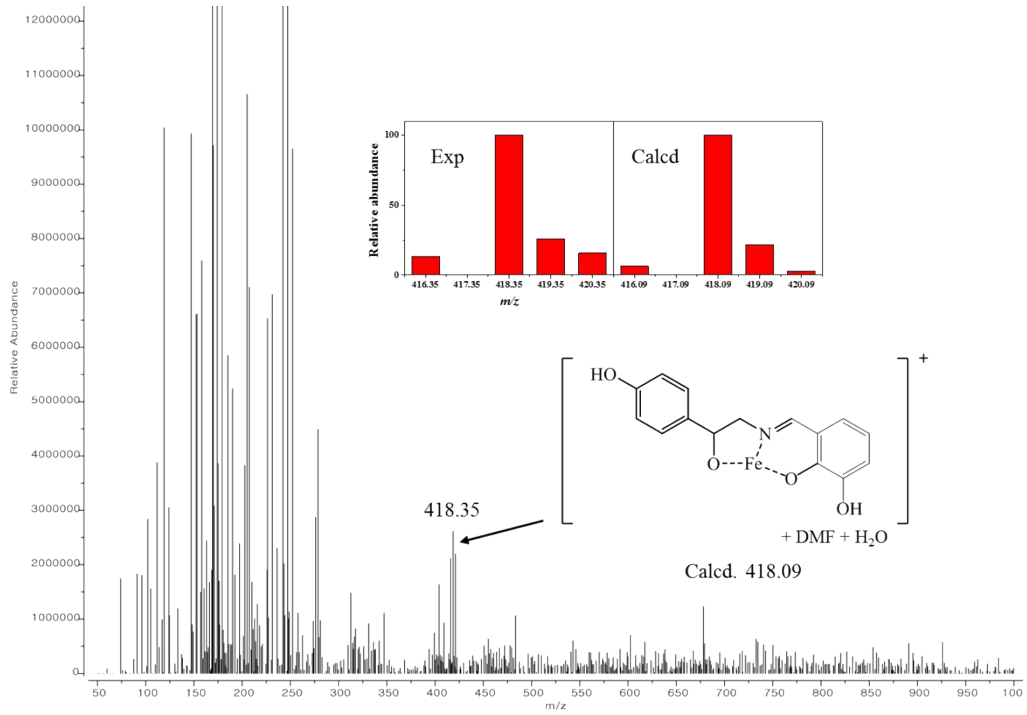

Fig. S4. Positive-ion ESI-mass spectrum of **1** (100 μM) in the presence of 1 equiv of $Fe(NO_3)_3$.

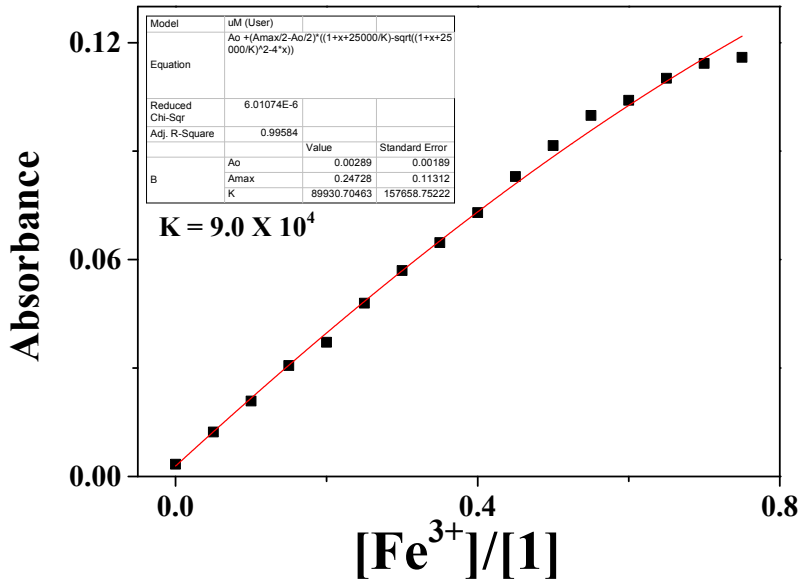

Fig. S5. The association constant of **1** toward Fe^{3+} using non-linear equation on the basis of UV-vis titration.

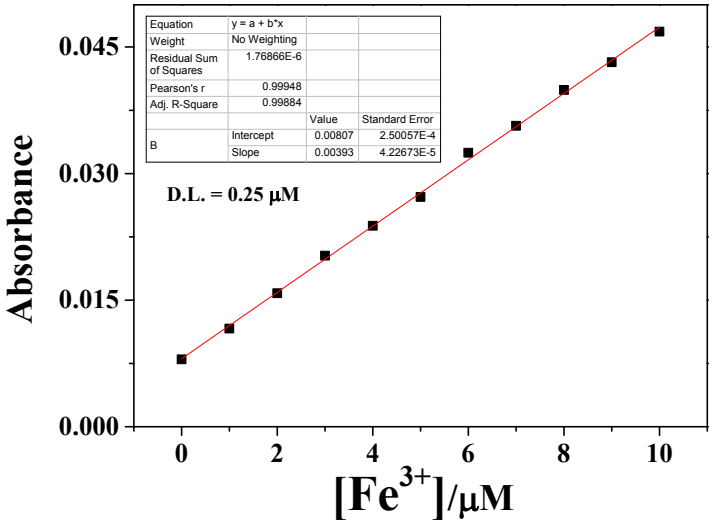

Fig. S6. The detection limit (*via* 3σ/slope) of **1** (40 μM) with Fe^{3+} on the basis of UV-vis titrations. σ means the average of the standard deviations.

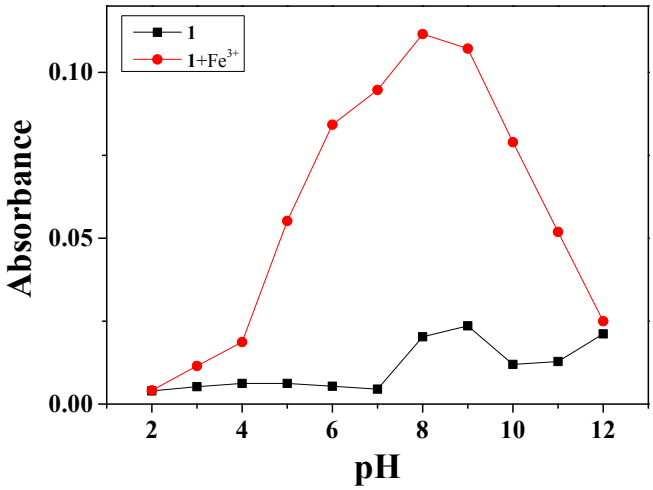

Fig. S7. Absorbance (at 500 nm) of **1** (40 μM) and **1**-Fe^{3+} complex (0.75 equiv) at pH range of 2-12.

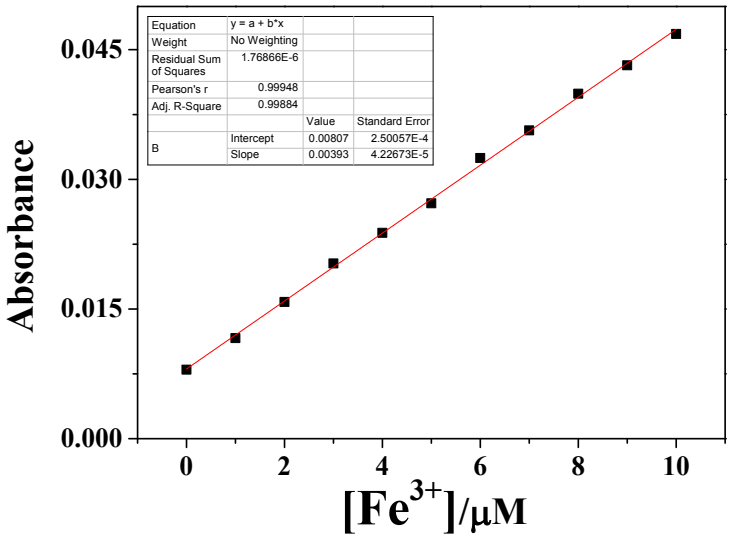

Fig. S8. The calibration curve (at 500 nm) of **1** upon the addition of Fe^{3+}. [**1**] = 40 μM and [Fe^{3+}] = 0.0–10.0 μM in buffer (bis-tris, 10 mM, pH = 7.0).

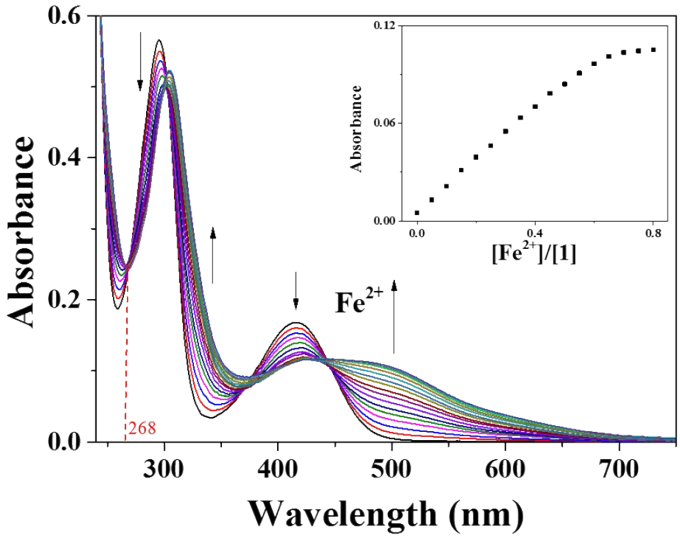

Fig. S9. UV-vis spectral changes of **1** (40 μM) as the different concentrations of Fe^{2+}. Inset: Plot of absorbance at 500 nm vs Fe^{2+} concentration.

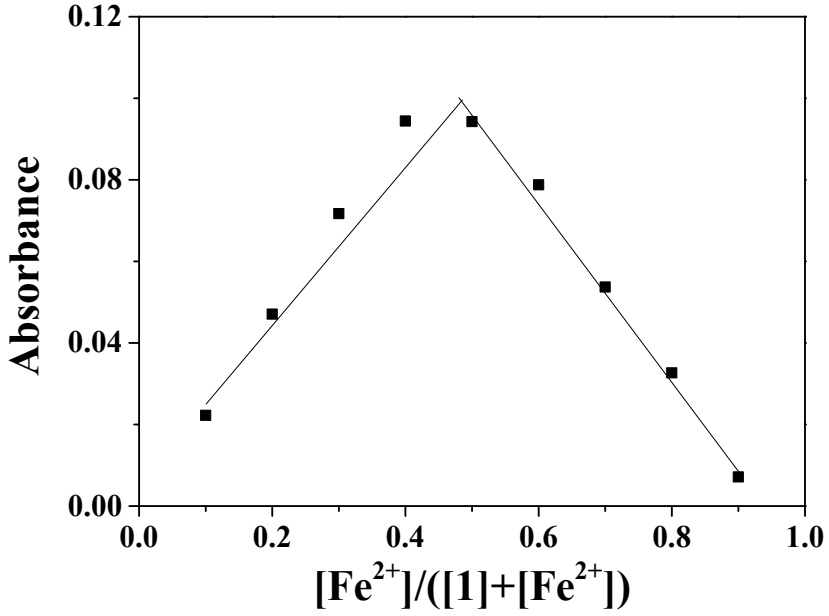

Fig. S10. Job plot for the binding ratio of **1** (80 μM) toward Fe^{2+} (80 μM).

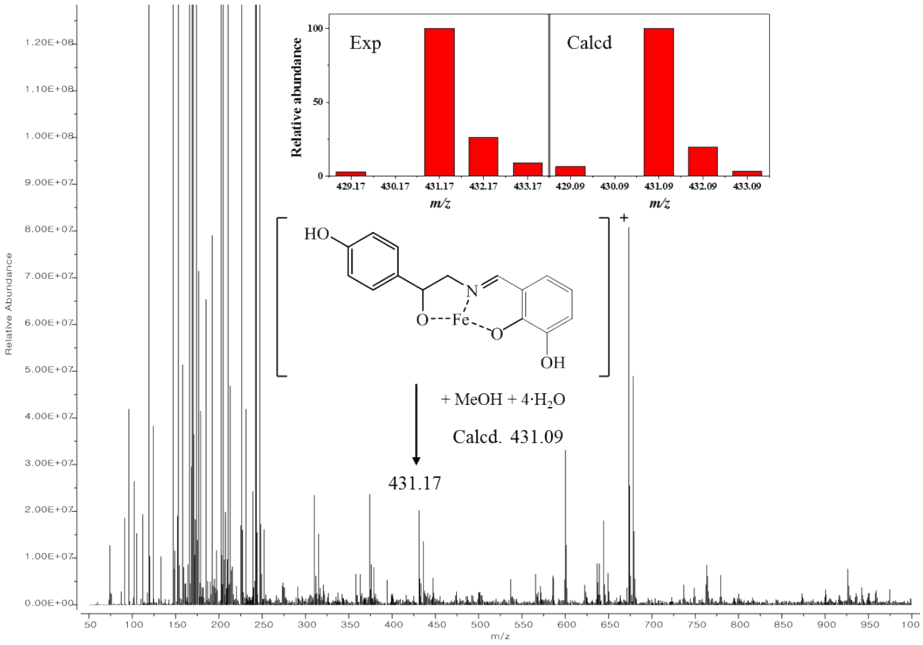

Fig. S11. Positive-ion ESI-mass spectrum of **1** (100 μM) in the presence of 1 equiv of $Fe(ClO_4)_2$.

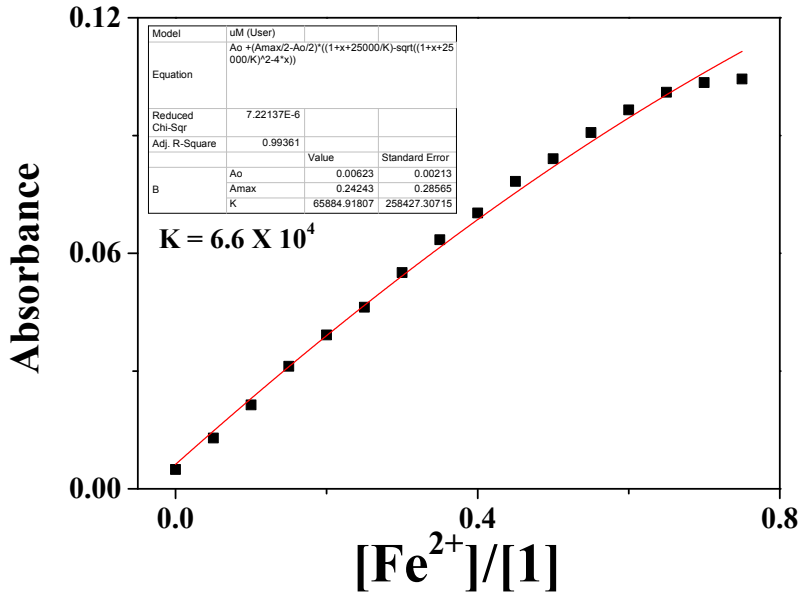

Fig. S12. The association constant of **1** toward Fe^{2+} using non-linear equation on the basis of UV-vis titration.

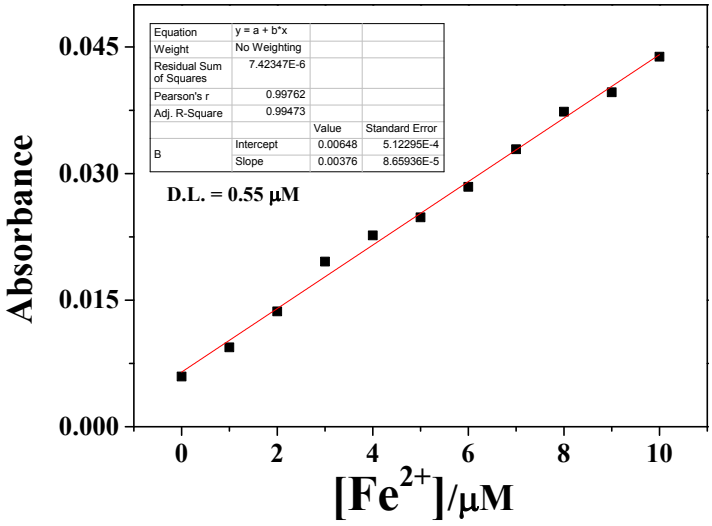

Fig. S13. The detection limit (*via* 3σ/slope) of **1** (40 μM) with Fe^{2+} on the basis of UV-vis titrations. σ means the average of the standard deviations.

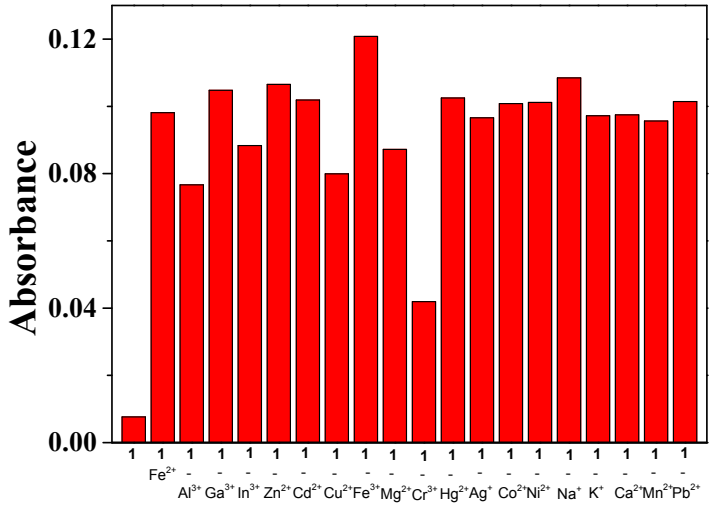

Fig. S14. Bar graphs of **1** (40 μM) for detection of Fe^{2+} in the presence of various metal ions in buffer (bis-tris, 10 mM, pH = 7.0).

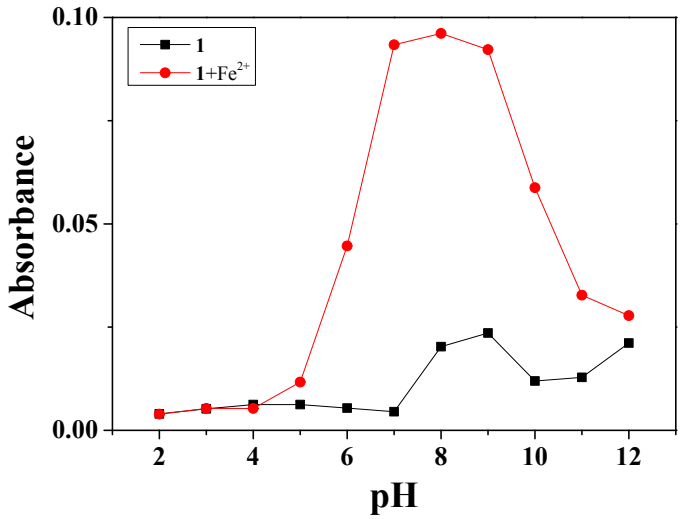

Fig. S15. Absorbance (at 500 nm) of **1** (40 μM) and **1**-Fe^{2+} complex (0.75 equiv) at pH range of 2-12.

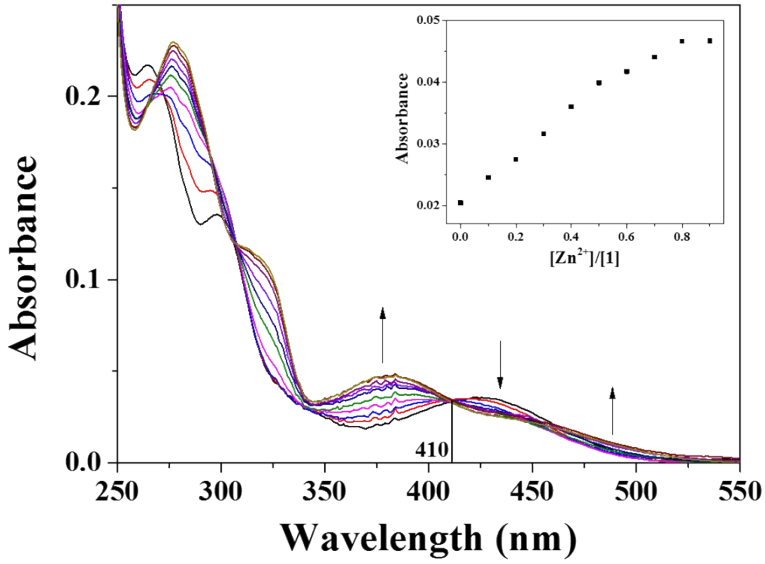

Fig. S16. UV-vis titrations of **1** (20 μM) in the change of Zn^{2+} concentrations. Inset: Plot of absorbance at 374 nm vs Zn^{2+} concentration.

.

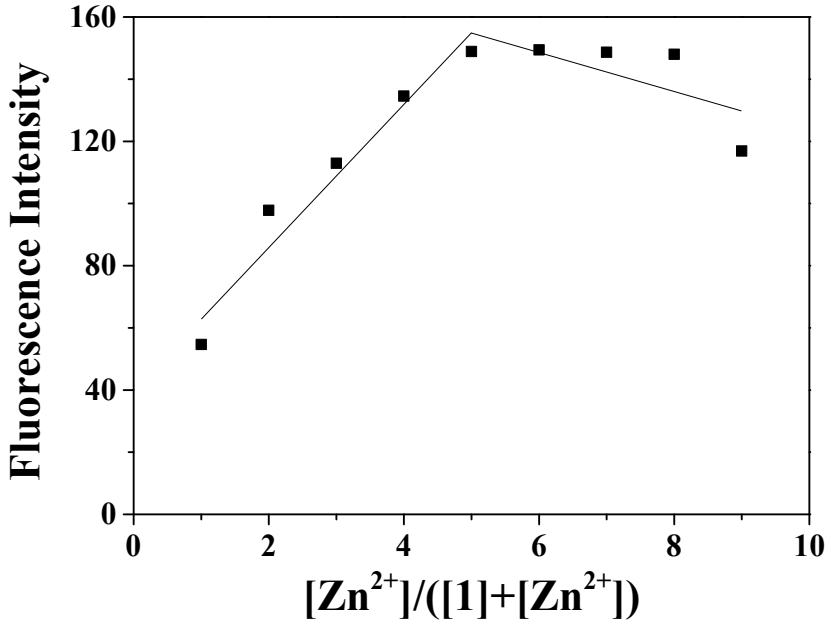

Fig. S17. Job plot for the binding ratio of **1** (100 μM) toward Zn^{2+} (100 μM).

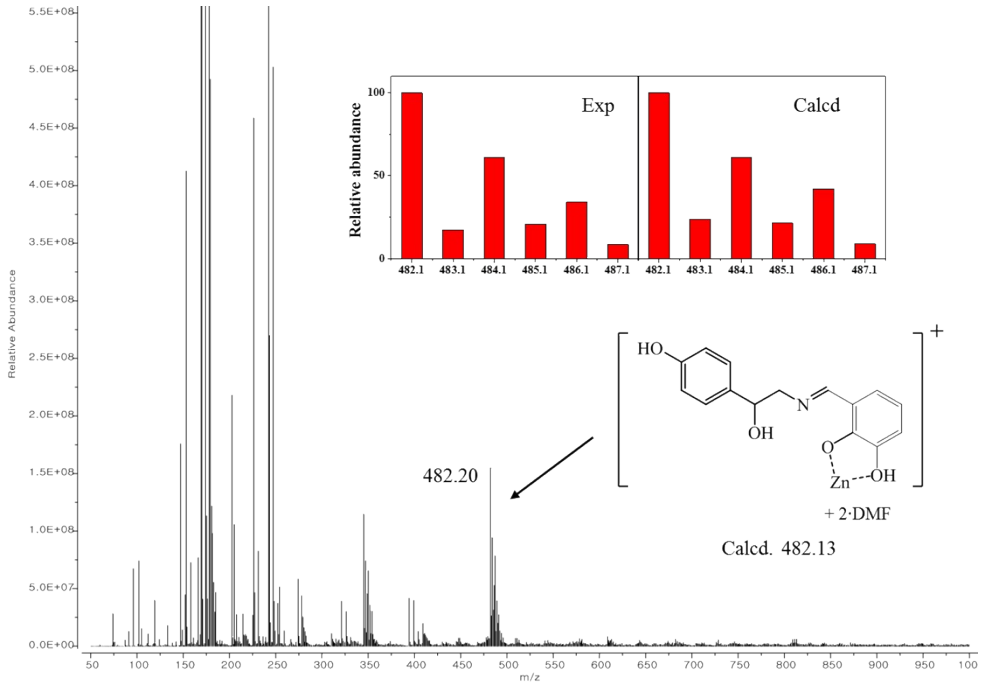

Fig. S18. Positive-ion ESI-mass spectrum of **1** (100 μM) in the presence of 1 equiv of $Zn(NO_3)_2$.

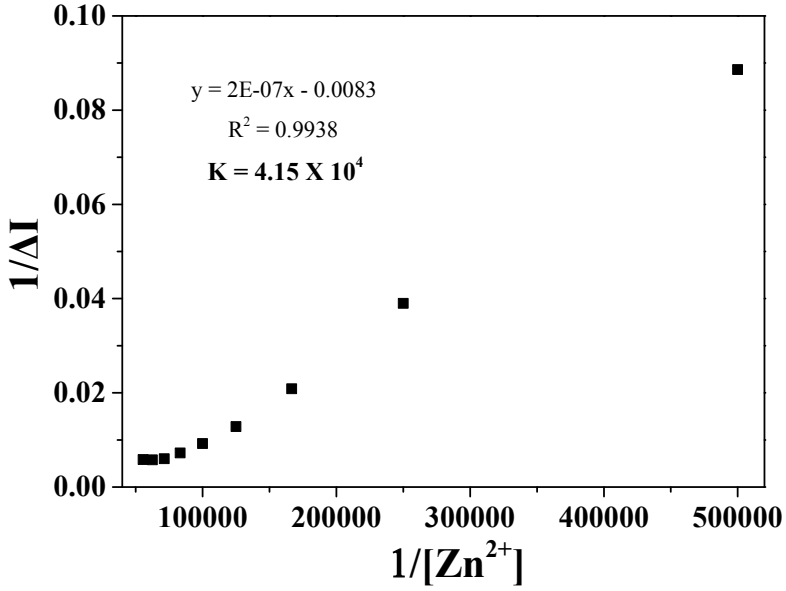

Fig. S19. The binding constant of **1** toward Zn^{2+} using Benesi-Hilderbrand equation on the basis of fluorescence titration.

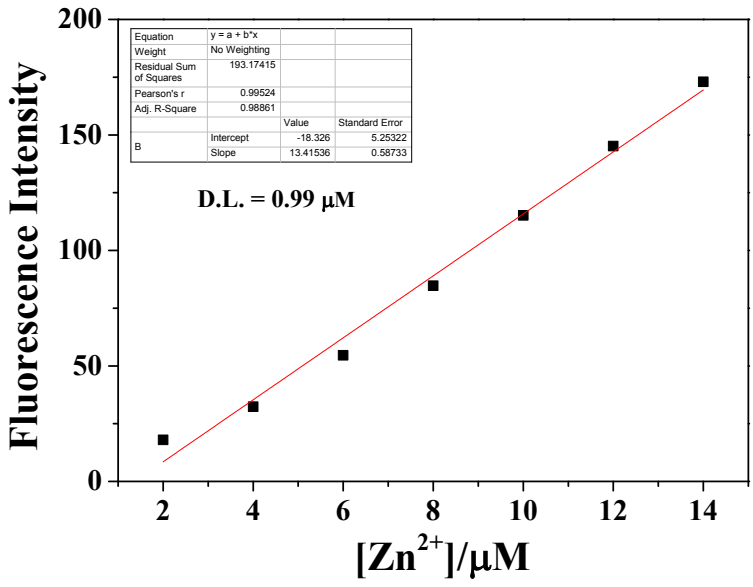

Fig. S20. The detection limit (*via* 3σ/slope) of **1** (20 μM) with Zn^{2+} on the basis of fluorescence titrations. σ means the average of the standard deviations.

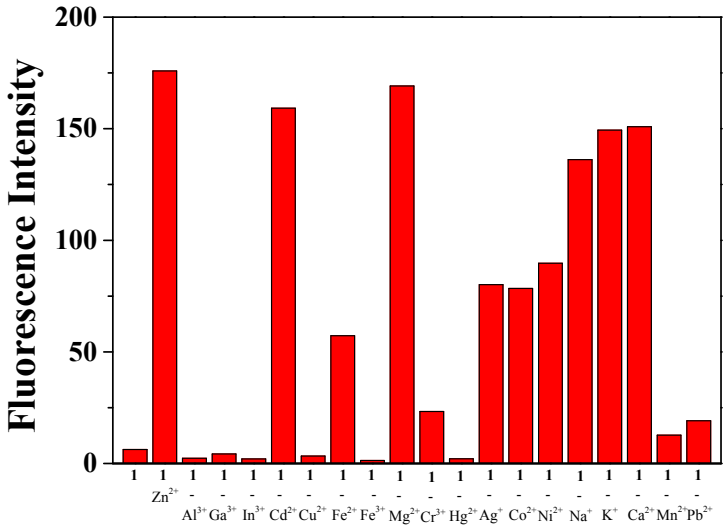

Fig. S21. Bar graphs (at 493 nm) of **1** (20 μM) for detection of Zn^{2+} in the presence of various metal ions.

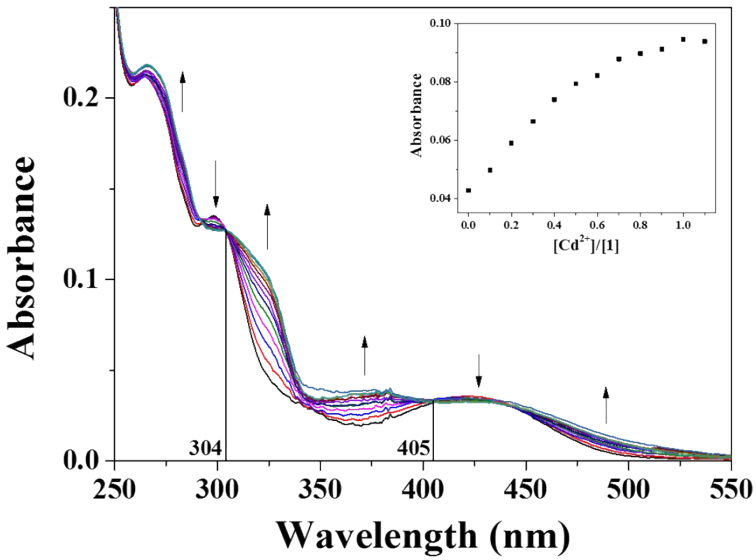

Fig. S22. UV-vis titrations of **1** (20 μM) in the change of Cd^{2+} concentrations. Inset: Plot of absorbance at 327 nm vs Cd^{2+} concentration.

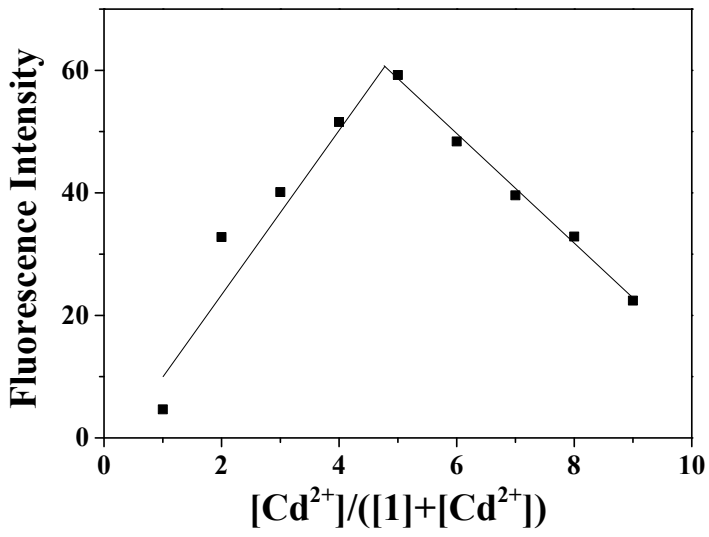

Fig. S23. Job plot for the binding ratio of **1** (100 μM) toward Cd^{2+} (100 μM).

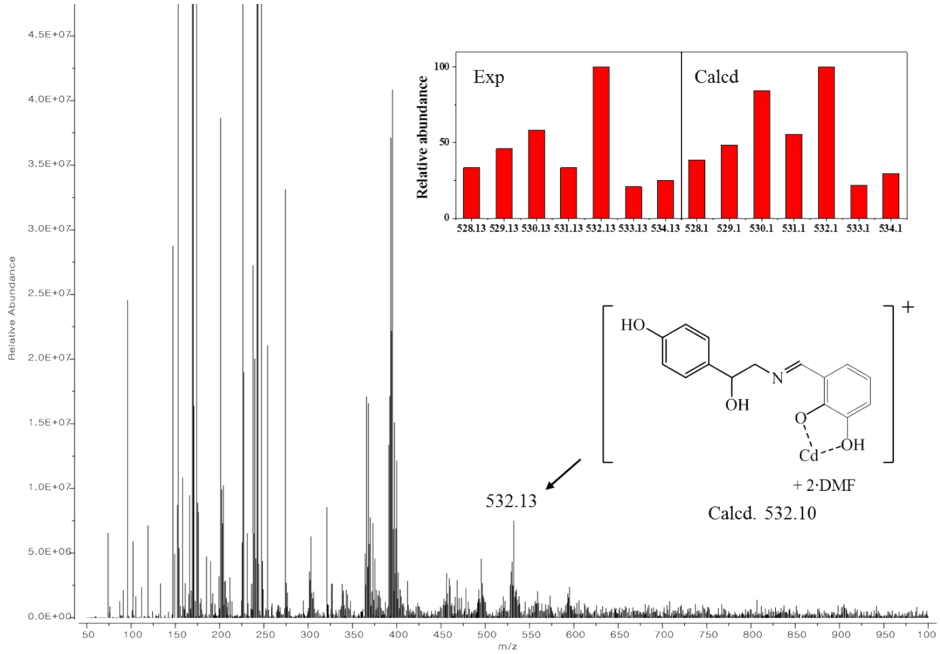

Fig. S24. Positive-ion ESI-mass spectrum of **1** (100 μM) in the presence of 1 equiv of $Cd(NO_3)_2$.

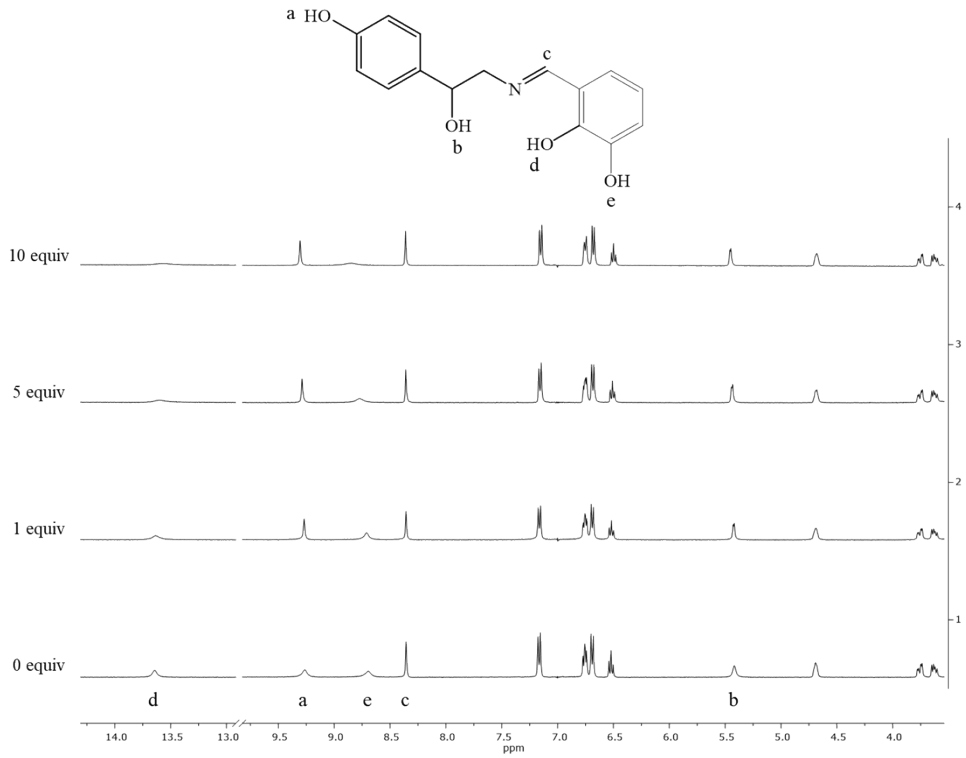

Fig. S25. ^{1}H NMR titrations of **1** with Cd^{2+} (0, 1, 5 and 10 equiv).

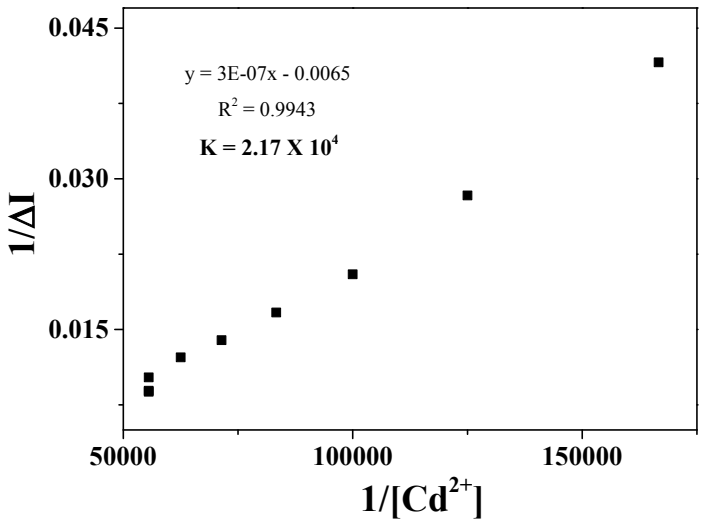

Fig. S26. The binding constant of **1** toward Cd^{2+} using Benesi-Hilderbrand equation on the basis of fluorescence titration.

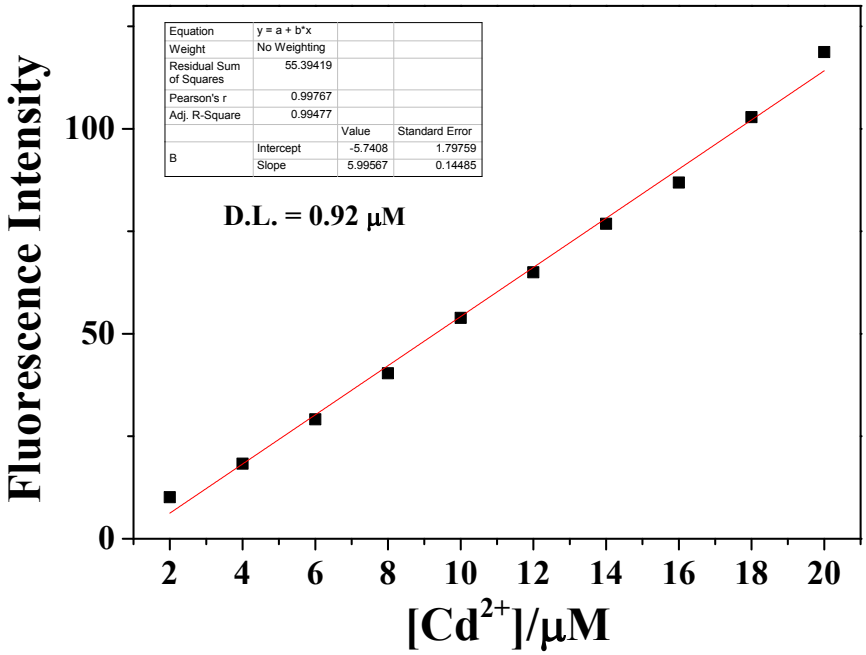

Fig. S27. The detection limit (*via* 3σ/slope) of **1** (20 μM) with Cd^{2+} on the basis of fluorescence titrations. σ means the average of the standard deviations.

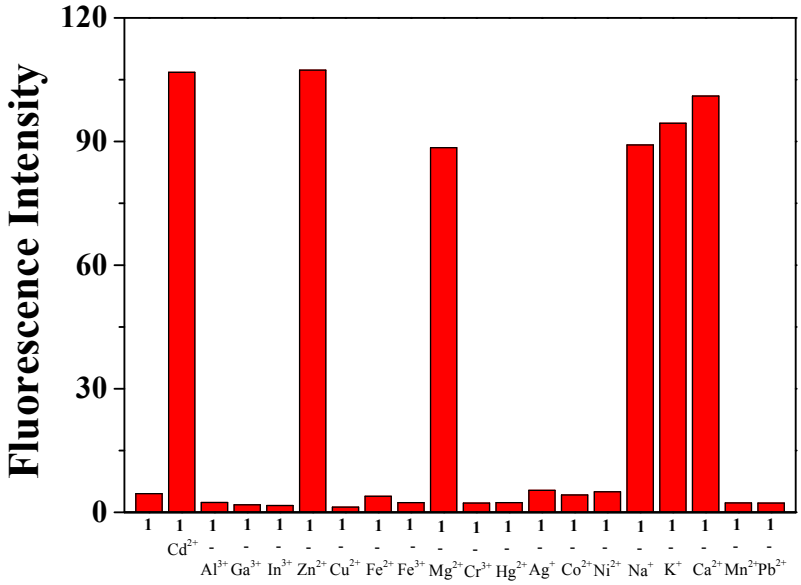

Fig. S28. Bar graphs (at 465 nm) of **1** (20 μM) for detection of Cd^{2+} in the presence of various metal ions.

(a)

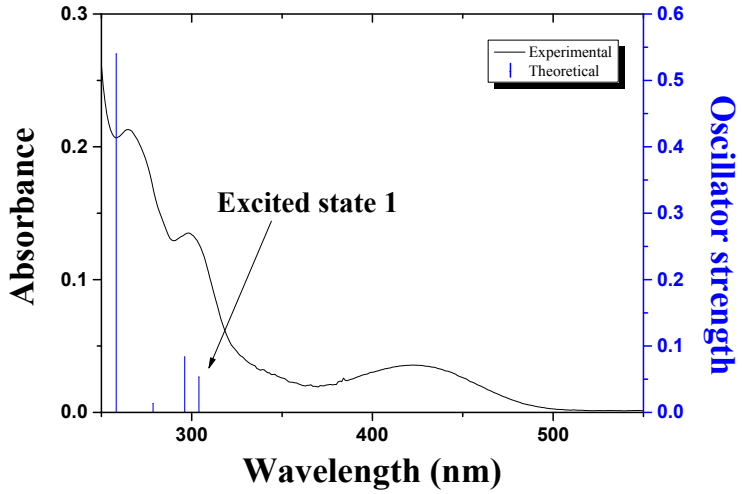

(b)

Excited state 1	Wavelength (nm)	Percent (%)	Main character	Oscillator strength
H-1 → L	303.96	73	ICT	0.0534
H → L		20	ICT	

Fig. S29. (a) The theoretical excitation energies and the experimental UV-vis spectrum of **1**. (b) The major electronic transition energy and molecular orbital contributions for **1** (H = HOMO and L = LUMO).

(a)

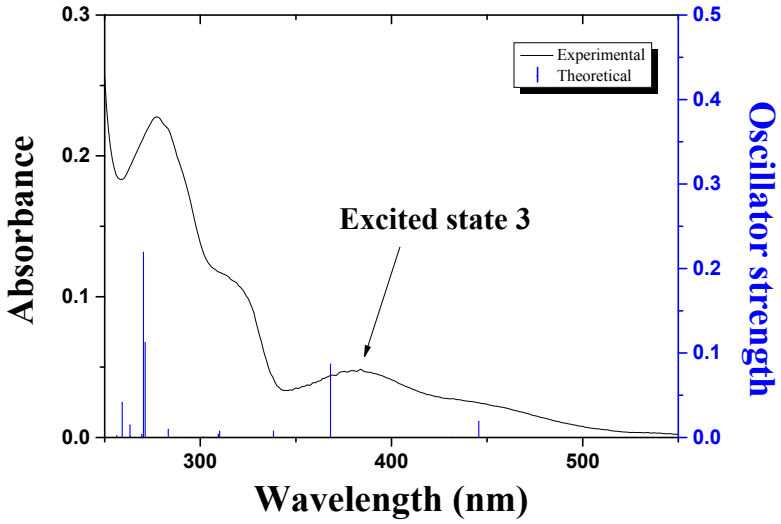

(b)

Excited state 3	Wavelength (nm)	Percent (%)	Main character	Oscillator strength
H → L+2	368.10	98	ICT	0.0867

Fig. S30. (a) The theoretical excitation energies and the experimental UV-vis spectrum of **1**-Zn^{2+}. (b) The major electronic transition energy and molecular orbital contributions for **1**-Zn^{2+} (H = HOMO and L = LUMO).

(a)

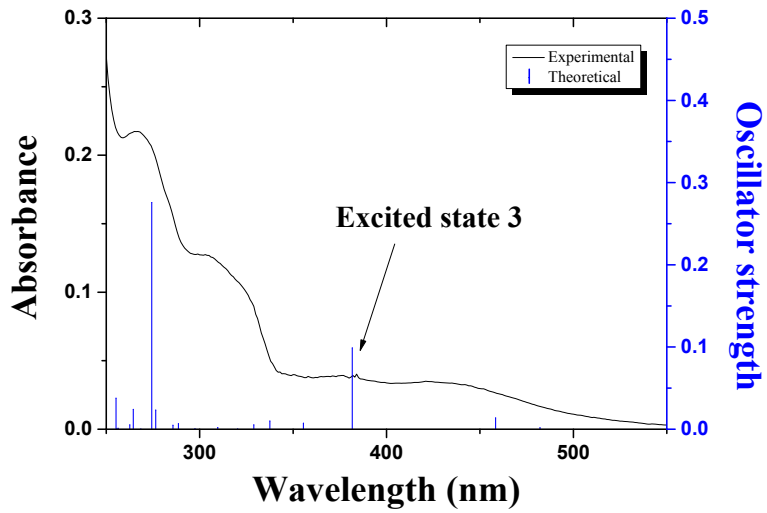

(b)

Excited state 3	Wavelength (nm)	Percent (%)	Main character	Oscillator strength
H → L+2	381.68	98	ICT	0.0989

Fig. S31. (a) The theoretical excitation energies and the experimental UV-vis spectrum of **1**-Cd^{2+}. (b) The major electronic transition energy and molecular orbital contributions for **1**-Cd^{2+} (H = HOMO and L = LUMO).

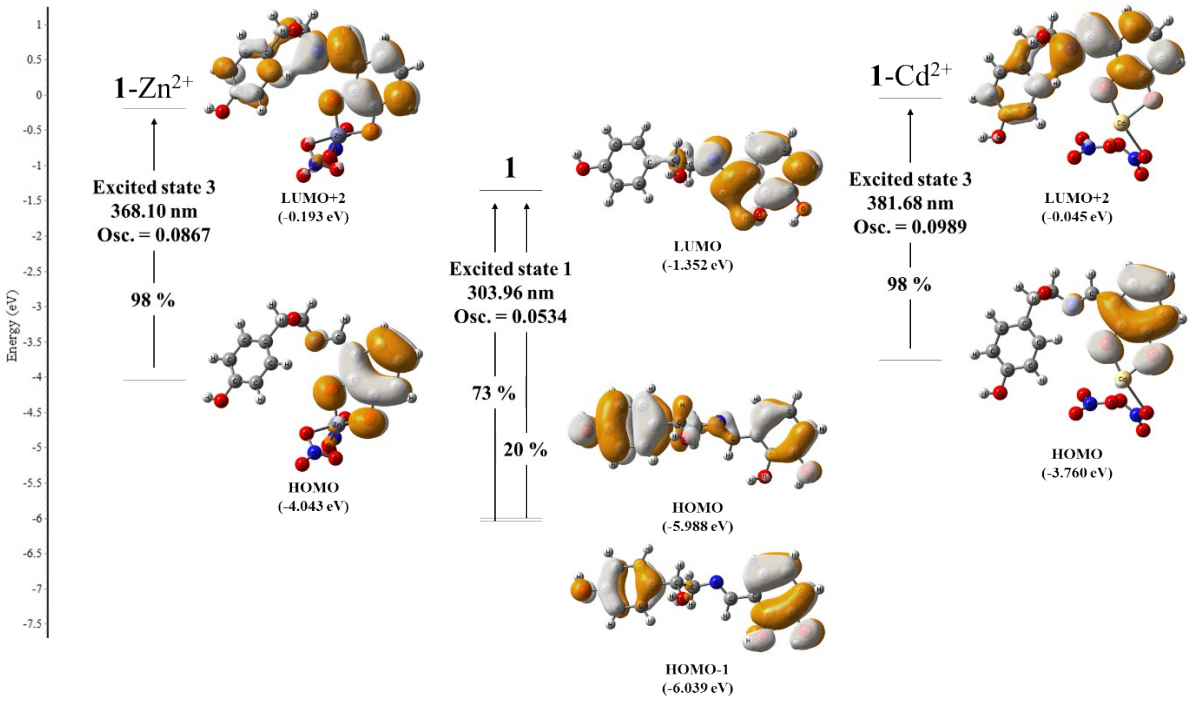

Fig. S32. MO diagrams and excitation energies of **1**, **1**-Zn^{2+} and **1**-Cd^{2+} by TD-DFT methods.